ADVANCED MATERIALS
www.advmat.de

One-Pot Synthesis of Multiple Protein-Encapsulated DNA Flowers and Their Application in Intracellular Protein Delivery

*Eunjung Kim, Limor Zwi-Dantsis, Natalie Reznikov, Catherine S. Hansel, Shweta Agarwal, and Molly M. Stevens**

Inspired by biological systems, many biomimetic methods suggest fabrication of functional materials with unique physicochemical properties. Such methods frequently generate organic–inorganic composites that feature highly ordered hierarchical structures with intriguing properties, distinct from their individual components. A striking example is that of DNA–inorganic hybrid micro/nanostructures, fabricated by the rolling circle technique. Here, a novel concept for the encapsulation of bioactive proteins in DNA flowers (DNF) while maintaining the activity of protein payloads is reported. A wide range of proteins, including enzymes, can be simultaneously associated with the growing DNA strands and Mg_2PPi crystals during the rolling circle process, ultimately leading to the direct immobilization of proteins into DNF. The unique porous structure of this construct, along with the abundance of Mg ions and DNA molecules present, provides many interaction sites for proteins, enabling high loading efficiency and enhanced stability. Further, as a proof of concept, it is demonstrated that the DNF can deliver payloads of cytotoxic protein (i.e., RNase A) to the cells without a loss in its biological function and structural integrity, resulting in highly increased cell death compared to the free protein.

Technological advances in DNA-based nanoscale construction, including hybridization-based DNA assembly (i.e., DNA origami, DNA tiles, etc.), nanoparticle-templated DNA assembly, and supramolecular DNA assembly, have enabled the fabrication of dynamic and complex DNA architectures with well-defined molecular structures and shapes.[1] A highly attractive feature of such constructs lies in the fact that they can be multifunctional by precisely positioning other bioactive molecular components at the nanometer scale on their tailored structure. These interesting properties combined with their biocompatibility and modularity facilitate the engineering of diverse assemblies of DNA constructs for medical applications. Thus, fully addressable DNA-based nanostructures have great potential to encapsulate, release, and transport molecular cargos into cells. Recently, numerous examples of tailor-designed DNA nanostructures have been reported as effective delivery carriers for anticancer drugs,[2] small interfering RNA (siRNA),[3] immunostimulatory CpG motif-containing DNA,[4] and proteins.[5] To enable practical uses of the structures made by DNA assembly, it is necessary to develop the techniques that can synthesize large scale quantities of DNA strands with desired sequences at low cost.[6]

A rapidly growing class of isothermal rolling circle techniques, termed rolling-circle amplification (RCA) and rolling-circle transcription (RCT), provides a potential solution since these enzymatic amplification methods offer a simple, rapid, and cost-effective strategy to produce significant amounts of long DNA or RNA strands by using DNA or RNA polymerases.[7] In both techniques, the polymerases commonly work on small circular template DNA and initiate the synthesis of the functional amplicons with exceptionally high efficiency that serve repeating complements of the circle sequences. The obtained RCA or RCT products are able to construct self-organized nucleic acid nanomaterials or metahydrogels, and can be used as templates for the periodic assembly of nanopieces or DNA staples.[8]

During the RCA and RCT processes, the polymer-like DNA strands present in the reaction mixture are likely to mediate the nucleation and growth of magnesium pyrophosphate inorganic crystals, leading to DNA–inorganic hybrid composites with interesting structural properties. Due to their morphological features, they have been named RNA or DNA microsponges,[9] DNA nanoflowers,[10] DNA nanoclews,[11] and DNA nanococoons.[12] These hybrid composites show great potential for biomedical applications. For instance, RNA or DNA microsponges encoded with therapeutic oligonucleotide sequences (i.e., antisense oligonucleotides and siRNA) have been reported to silence genes in tumor cells for cancer

Dr. E. Kim, Dr. L. Zwi-Dantsis, Dr. N. Reznikov, C. S. Hansel, S. Agarwal, Prof. M. M. Stevens
Department of Materials
Department of Bioengineering and Institute for Biomedical Engineering
Imperial College London
London SW7 2AZ, UK
E-mail: m.stevens@imperial.ac.uk

DOI: 10.1002/adma.201701086

treatment.[9] Small molecules (i.e., dye, drug, and aptamer)-incorporated DNA nanoflowers can potentially be utilized for targeted drug delivery and imaging.[10a,b] Moreover, enzyme capsules have been attached to enzyme-degradable DNA nanoclews or nanococoons: the released enzyme digests the DNA strands in a nonspecific or specific way, promoting the release of therapeutics contained within nanoclews or nanococoons.[12,13] However, within this context, a less-explored aspect of RCA-based DNA constructs is to address the unique local environment created within the DNA particle that provides negatively charged phosphate pools along with abundant magnesium ions, which may serve as specific binding sites for biomolecules with additional effects. Indeed, using a DNA structure to efficiently encapsulate biomolecules, especially enzymes, has been shown to markedly enhance the enzyme activity and stability by virtue of an environment full of negative charges.[14] This approach involves two steps for enzyme encapsulation with well-defined 3D DNA origami scaffolds, but to our knowledge, the entrapment of a wide range of proteins in a 3D DNA structure through a one-pot synthesis has never been reported.

Here, we report a new approach that directly synthesizes protein-encapsulated DNA flowers (DNF) with biological activity, in which the RCA reaction is carried out in the presence of proteins (**Figure 1**a). The protein molecules are thus spontaneously incorporated into the growing DNA strands and magnesium pyrophosphate (Mg_2PPi) inorganic crystals produced during RCA. Such a method is potentially generic and distinct from multistep encapsulation approaches using postsynthetic modification, where the intact or chemically modified proteins are noncovalently immobilized to the presynthesized DNA particles.[11–13,15] Therefore, our methodology greatly expands the selection of diverse proteins, where its experimental simplicity and moderate reaction conditions in an aqueous medium make it highly promising for biological applications. We further exploited the potential of this technique as a protein delivery system by demonstrating that the encapsulation of cytotoxic proteins in DNF can induce considerable toxic effects against cells.

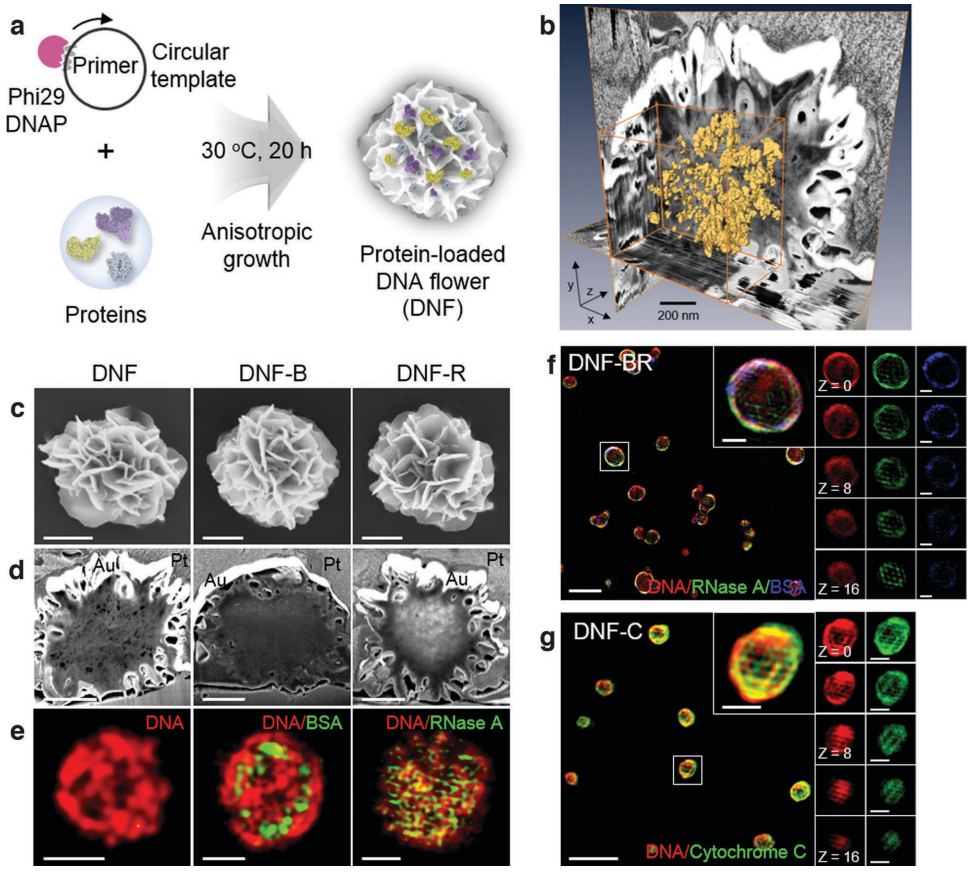

Figure 1. Synthesis of protein-encapsulated DNA flowers (DNF). a) Schematic illustration of encapsulating proteins in DNF via rolling circle amplification (RCA). b) Three-dimensionally reconstructed internal nanopores (yellow) in DNF using dual beam microscope (FIB-SEM). The orange box indicates the position of the region of interest (880 nm × 870 nm × 255 nm) chosen for 3D rendering of the pores. c) Scanning electron microscopy (SEM) images, d) FIB-SEM images of orthogonal cross-sections, and e) structured illumination microscopy (SIM) images of DNF (left), DNF-B (middle), and DNF-R (right). In the FIB-SEM images, the protective platinum (Pt) layer and gold (Au) coating on each sample are indicated. For SIM imaging, DNA was labeled with Cy3 (red) and BSA and RNase A were labeled with fluorescein (green), respectively. Scale bar, 500 nm (top and middle), 1 µm (bottom). f) SIM images of DNF containing both BSA and RNase A (DNF-BR) and g) DNF containing cytochrome C (DNF-C). DNA, RNase A or cytochrome C, and BSA were labeled with Cy3 (red), fluorescein (green), and CF 405M (blue), respectively. Insets indicate higher magnification views of the white rectangular region in the main image. Individual frames of z-stacks (step size: 0.1 µm) of the inset particle are shown in the right panel. Scale bar, 5 µm (main panels), 1 µm (inset and right panels).

To fabricate protein-containing DNF, we chose bovine serum albumin (BSA) as a control protein and bovine pancreatic ribonuclease A (RNase A) as a cytotoxic protein. While BSA is a relatively large protein with molecular dimensions of 4 nm × 4 nm × 14 nm and an isoelectric point (pI) of 4.9,[16] RNase A is a small enzyme with molecular dimensions of 2.2 nm × 2.8 nm × 3.8 nm and a pI of 9.6.[17] Due to the ribonucleolytic activity of RNase A, it degrades its substrate RNA molecules which reside in the cytosol when it enters the cells, subsequently causing cell death. Its cytotoxicity is often hindered by potent cytosolic ribonuclease inhibitors that shield the access of substrates to the active sites of RNase A.[18] Therefore, RNase A can serve as an ideal model for assessing the protein delivery system using DNF.

For RCA, we first prepared circular template DNA by ligation of 5′-phosphorylated linear DNA with T4 DNA ligase and additional treatment with exonuclease I to remove noncircularized template DNA or excess primers. Both native and denatured polyacrylamide gel electrophoresis (PAGE) confirmed the successful circularization of template DNA combined with a primer, yielding the reduced mobility relative to the linear analog (Figure S1, Supporting Information). The RCA was then achieved in a solution (50 µL) containing circular template DNA (0.6×10^{-6} M), deoxynucleotides (dNTPs) (1×10^{-3} M), and phi29 DNA polymerase (phi29 DNAP) (1 U µL^{-1}) in the reaction buffer at 30 °C (Figure S2a, Supporting Information). The DNF were collected by centrifugal separation and washing of the RCA products with nuclease-free water. In a typical isothermal RCA reaction, both the enzymatic reaction and the crystallization need to be taken into consideration as the DNA strands, which are mainly synthesized by phi29 DNAP consuming dNTPs, and the Mg_2PPi by-products are produced at the same time.[19] Indeed, the concentrations of DNA and PPi in the DNF gradually increase over time and are almost saturated at 20 h, giving rise to time-dependent changes in their morphology and size (Figure S2b–j, Supporting Information). As shown in the scanning electron microscopy (SEM) images at different time points, spherical nanoparticles with smooth surfaces were seen at the early stage and continuously grew up in the following 16 h, reaching a size of 1–2 µm. At 20 h, further anisotropically controlled growth led to a relatively monodisperse set of flower-like particles and a prolonged incubation of 30 h showed no appreciable differences compared to 20 h incubation. Therefore, we selected the DNF obtained at 20 h, containing sufficient amounts of DNA and PPi for effective loading of protein cargos.

In order to investigate the internal structure of the DNF more closely, we performed 3D tomography of the pores with a stack of 50–60 slices (slice thickness, ≈4 nm) using a dual beam microscope (focused ion beam (FIB)-SEM) and the serial surface view (SSV) method.[20] This method involves the serial sectioning of a thin layer from the sample surface using a FIB and the simultaneous imaging of the exposed cross-sections using SEM, allowing the collection of serial cross-sectional slices for 3D reconstructions. Movie S1 (Supporting Information) and Figure 1b show corresponding segmented images from the FIB-SEM serial sectioning, along with a 3D view of DNF with reconstructed pores. This confirms the existence of well-developed nanopores that are evenly spread throughout the particle. The DNF possesses ≈4.5% of the pore volume fraction, in which its pore capacity (or the pore volume, 2.4×10^7 nm^3, assuming that the average diameter of the DNF is 1 µm) can accommodate up to $\approx 10^5$ BSA molecules or $\approx 10^6$ RNase A molecules. Thus, the FIB-SEM analysis of DNF provides profound insight into their internal porous nature, which is distinct from the previous reports that have largely focused on surface morphology.

Next, we fabricated DNF containing BSA and RNase A by simply adding each protein solution (0.6 mg mL^{-1}) to the RCA reaction mixtures (termed DNF-B and DNF-R, respectively, hereafter), followed by several washes with nuclease-free water. Figure 1c,d and Figure S3 (Supporting Information) present the SEM and FIB-SEM images of the synthesized DNF, DNF-B, and DNF-R and reveal that protein encapsulation does not make a discernible difference in the morphology and size of the DNF but influences their porosity. This deformation of the internal structure is further observed in multiple slices of FIB-SEM images, most likely due to noncovalent adsorption between proteins and charged DNA strands (Movies S2 and S3, Supporting Information).

To detect each protein within the DNF, we employed structured illumination microscopy (SIM), a super-resolution technique that resolves objects with about 100 nm spatial resolution in the lateral dimension[21] and characterized the fluorescence colocalization of Alexa Fluor 488-conjugated BSA or fluorescein-conjugated RNase A and Cy3-labeled DNF. In cross sections of 3D SIM image stacks, we found that each protein strictly localizes within the DNA matrix throughout the DNF (Figure 1e, and Figure S4 and Movies S4 and S5, Supporting Information). More interestingly, DNF-B and DNF-R showed clearly different protein localization, where BSA was predominantly located on the periphery of the particle surface, while RNase A was evenly distributed throughout the particle. Given that BSA is negatively charged and RNase A is positively charged at neutral pH, which is the pH condition of the RCA reaction, we hypothesized that electrostatic interactions govern the protein adsorption to negatively charged DNA molecules while growing into the DNF.

To test the consistency of protein distribution, we prepared both proteins-embedded fluorescent DNF (DNF-BR) by including CF 405M-tagged BSA and fluorescein-labeled RNase A and conducted SIM imaging. As expected, the obtained images showed similar distribution patterns to that of single protein-loaded DNF (Figure 1f). Moreover, we examined DNF containing cytochrome C (DNF-C), another protein that has shown an intermediate role in apoptosis and has a pI of ≈10 with a molecular size of 3 nm × 3.4 nm × 3.4 nm, making it positively charged at neutral pH.[22] Consistent with DNF-R, we observed that cytochrome C is homogeneously scattered in DNF (Figure 1g), supporting our hypothesis that protein adsorption is mediated by electrostatic interactions. In addition to this, we speculate that magnesium would mediate bridging between DNA and proteins through coordinative interactions because of its ability to form complexes with carboxylates of protein residues, phosphate backbones of nucleic acids, and water by inner or outer sphere coordination.[23] Therefore, the multiple interactions involved during RCA may facilitate the protein embedding, particularly BSA loading into the DNF,

although strong electrostatic repulsion between BSA and DNA molecules would occur as a result of their same charge.

We further characterized the structures and compositions of DNF and protein-containing DNF by chemical mapping using a transmission electron microscope (TEM) operating in scanning transmission electron microscope (STEM) mode combined with energy dispersive X-ray spectroscopy (EDS) (**Figure 2**a–d). The high-angle annular dark-field STEM (HAADF-STEM) images revealed their porous and hierarchical structure, as observed in the SEM images. The STEM-EDS elemental mapping and spectra confirmed the existence of carbon, nitrogen, oxygen, magnesium, and phosphorus in these formulations, which mainly consist of DNA, proteins, and Mg_2PPi. Merging the distribution of carbon and nitrogen with magnesium demonstrates that the particles had carbon and nitrogen-abundant shells, which indicates that organic materials of DNA and proteins are trapped in the shells to form the DNF or protein-DNF. The average atomic ratios of carbon, nitrogen, and oxygen to magnesium in DNF-B and DNF-R were higher than DNF, whereas the ratio of phosphorus to magnesium remained almost the same, which can be attributed to the addition of proteins in the DNF (Figure 2e).

To detect protein and DNA in the protein-containing DNF, we also carried out sodium dodecyl sulfate PAGE (SDS-PAGE) and agarose gel electrophoresis (**Figure 3**a). A protein band corresponding to the molecular weight of monomeric BSA (66.5 kDa) or RNase A (13.7 kDa) was shown on the gel for both free protein and protein-containing DNF (lanes 1 and 3 for BSA, lanes 6 and 8 for RNase A, respectively). Furthermore, a phi29 DNAP band at around 66.7 kDa with very weak band intensity was observed in the DNF regardless of the loading proteins (lanes 2, 3, 7, and 8), confirming nonselective encapsulation of proteins in the DNF. Nevertheless, the existence of DNAP in the DNF would not interfere with the performance of

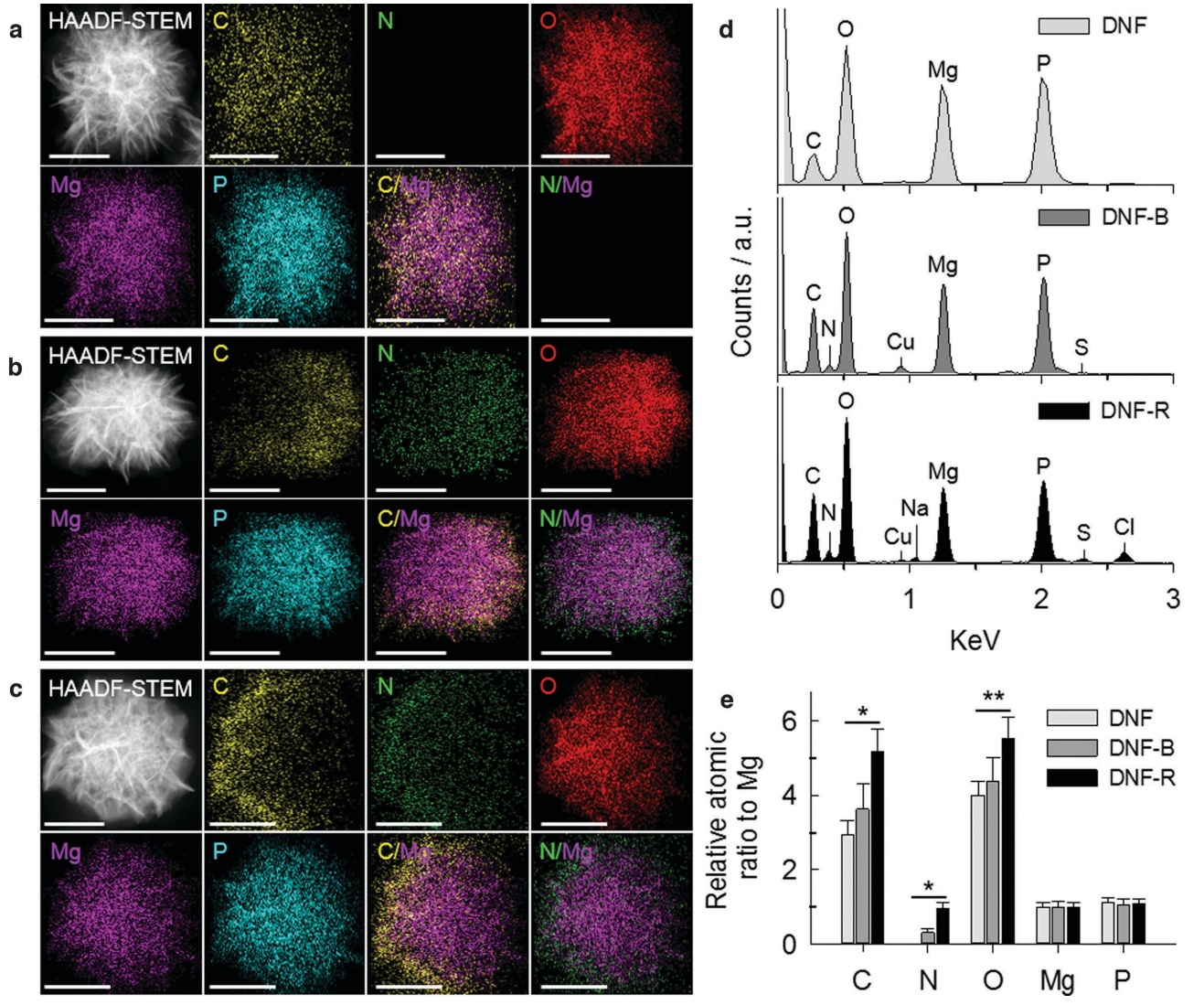

Figure 2. STEM-EDS analysis of protein-entrapped DNF. Representative HAADF-STEM images and EDS elemental mapping (C, N, O, Mg, and P) of a) DNF, b) DNF-B, and c) DNF-R. Merged images of C and Mg maps and N and Mg maps were shown. Scale bar, 500 nm. d) EDS spectra recorded from the whole area of the individual particle. e) Relative atomic ratios of each element to Mg in DNF, DNF-B, and DNF-R. Data represent mean ± s.d. of the EDS measurements determined over five particles. $^*P < 0.001$ and $^{**}P < 0.05$ based on one-way ANOVA and Tukey test's multiple comparison test.

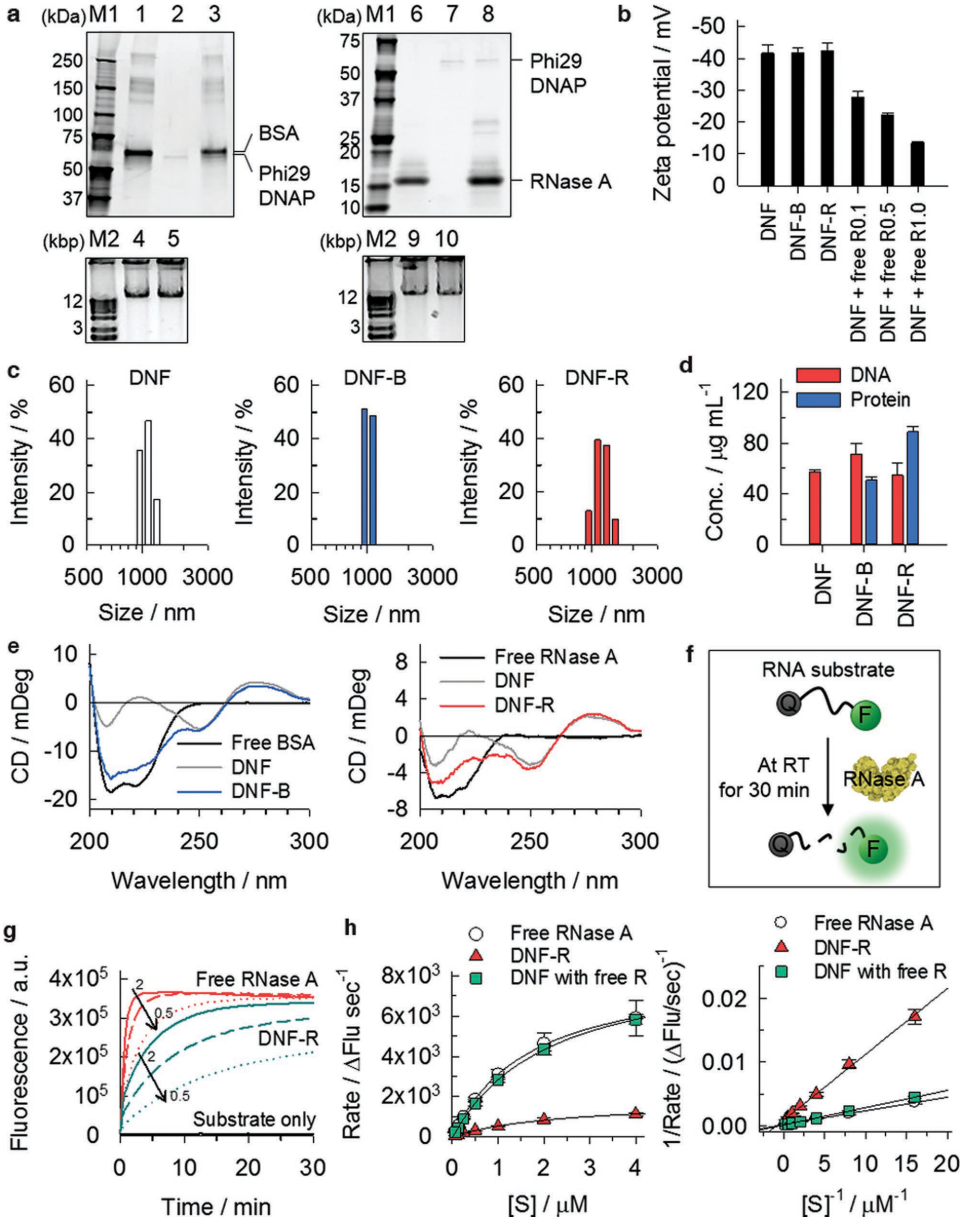

Figure 3. Characterization of protein-containing DNF. a) SDS-PAGE (top) and agarose gel electrophoresis (bottom) analysis. Lane M1: protein marker, lane M2: 1 kbp DNA marker, lane 1: free BSA, lanes 2, 4, 7, and 9: DNF, lanes 3 and 5: DNF-B, lane 6: free RNase A, lanes 8 and 10: DNF-R. b) Zeta potentials of DNF, DNF-B, DNF-R, and the mixtures of DNF and various concentrations of RNase A (0.1, 0.5, and 1.0 mg mL^{-1}). c) Size distribution of DNF, DNF-B, and DNF-R. d) Quantification of DNA and protein concentrations in DNF, DNF-B, and DNF-R. e) Circular dichroism (CD) spectra of free BSA, free RNase A, DNF, DNF-B, and DNF-R. The CD was measured in 20×10^{-3} M Tris–HCl buffer (pH 8.0) at 25 °C. f) Schematic illustration of an enzyme activity assay using the RNA substrate modified with a fluorescein dye (F) and a quencher (Q) at both ends. After enzyme cleavage, the fluorescence emitted from the RNA substrate is indicative of the catalytic activity. Therefore, it was monitored over 30 min at λ_{ex} = 490 nm and λ_{em} = 520 nm. g) Catalytic kinetics of free RNase A and DNF-R with various enzyme concentrations (0.5, 1, and 2 ng mL^{-1}). The RNA substrate only (2×10^{-6} M) was used as a negative control. h) Michaelis–Menten (left) and Lineweaver–Burk (right) plots of free RNase A, DNF-R, and the mixture of RNase A and DNF (1 ng mL^{-1} of RNase A and 1.3 ng mL^{-1} of DNA). Results represent mean ± s.d. of two independent experiments.

the protein payloads as it was thermally denatured after the reaction. As shown in the agarose gel images, the DNA amplicons (>12 kbp) were detected in all samples (lanes 4, 5, 9, and 10), implying that the introduction of proteins during the formation of the particles did not impede RCA-based nucleic acid amplification. The prepared DNF, DNF-B, and DNF-R had similar zeta potentials of −42.7 ± 1.8, −42.5 ± 1.0, and −43.0 ± 1.8 mV, respectively (Figure 3b). However, the addition of free RNase A to the DNF via adsorption, not encapsulation, showed a gradual decrease in the zeta potential with increased enzyme concentration and resulted in particle aggregation when the concentration reached 1 mg mL^{-1}. This is because the RNase A molecules carrying positive charges caused nonspecific charge attraction with DNF. On the other hand, this reflects that our

strategy offers a stable protein delivery carrier without inducing particle aggregates in the fabrication scheme. The average size of these particles measured by dynamic light scattering was consistent with the SEM and TEM results (Figure 3c).

For quantification, we determined the amount of DNA and proteins based on calibration curves using the commercial assay kits (Figure 3d). The addition of BSA actually increased the yield of DNA product (1.2-fold) compared to RCA without additional proteins, likely as a result of its beneficial effect on enzymatic reactions such as the polymerase chain reaction.[24] In contrast, DNF-R had a slightly decreased DNA product (0.9-fold), signifying that RNase A may have some inhibitory effects on RCA due to possible binding to template DNA or DNA amplicons. Based on the measured protein concentration, the encapsulation efficiency and loading capacity of each protein were determined to be 52.4% and 71.5 g g^{-1} DNA for DNF-B and 91.4% and 163.5 g g^{-1} DNA for DNF-R, respectively. Furthermore, if the DNF are stained with a dye, individual DNF can be visible as a small fluorescent dot under fluorescence microscopy imaging. Therefore, counting the number of the fluorescent dots would be an effective means of quantifying the particle concentrations,[25] and thus the particle concentration and the DNA amount required for constructing each particle were listed in Table S1 (Supporting Information). In the circular dichroism (CD) spectra of DNF-B and DNF-R, they exhibited both characteristic protein peaks in the range of 210–222 nm[26] and DNA peaks at 245 and 280 nm,[27] compared with native proteins and free DNF (Figure 3e). This suggests the encapsulated protein retains its secondary structure, which is essential for preserving its catalytic activity.

To evaluate the activity of RNase A upon encapsulation within the DNF, we used a synthetic RNA oligonucleotide modified with fluorescein and a quencher at both ends. In the presence of RNase A, the RNA substrate was cleaved by the enzyme, producing a strong fluorescence signal (Figure 3f). As shown in Figure 3g, the overall activity of the entrapped RNase A in DNF-R was 1.2–1.6-fold lower than the free enzyme at the same enzyme concentration. The kinetic parameters, K_m and V_{max}, derived from the Michaelis–Menten and Lineweaver–Burk plots (Figure 3h) were shown in **Table 1**. This demonstrates that the K_m varied little between the encapsulated and free RNase A, indicating that the porous DNF structure did not hinder the enzyme affinity with the substrates. However, DNF-R exhibited a ≈10-fold decrease in the V_{max} compared to free enzyme, implying a reduction in enzyme flexibility for catalysis. In a control experiment, the mixture of DNF and RNase A via physical adsorption had a similar catalytic performance compared to free enzyme, suggesting that two plausible events may be responsible for the decrease in activity of the DNF-R: (1) multiple interactions between RNase A and the microenvironments of the DNF, which mainly contains not only highly concentrated magnesium ions with coordination ability but also DNA molecules, thereby leading to an unfavorable change in enzyme conformation and/or (2) possible thermal and/or chemical denaturation of RNase A in the synthetic process. Enzyme confinements into solid supports usually offer enhanced stability, but show lower activity than free enzymes.[28] This is mostly due to the loss of activity during the encapsulation process and the mass transfer limitations inducing a decrease in reaction rate and undesirable product accumulation.

Table 1. Kinetic data showing the Michaelis–Menten constant (K_m) and maximum velocity (V_{max}) of free RNase A, DNF-R, and the mixture of RNase A and DNF.

Sample	K_m[a] [μM]	V_{max}[a] [ΔFlu s^{-1}]
Free RNase A	2.2 ± 0.3	11137.3 ± 1608.4
DNF-R	1.2 ± 0.2	1180.6 ± 98.2
DNF with free RNase A	3.9 ± 0.2	12982.1 ± 584.1

[a]Data represent mean ± s.d. for two independent experiments.

Especially, a specific reaction buffer (50×10^{-3} M Tris–HCl, 10×10^{-3} M $MgCl_2$, 10×10^{-3} M $(NH_4)_2SO_4$, 4×10^{-3} M dithiothreitol, pH 7.5) and an optimized reaction condition (incubation at 30 °C for 20 h) are required for RCA using phi29 DNAP, allowing us to study the effects of the carryover reaction components, reaction temperatures, or addictive components (such as free DNF and Mg_2PPi) on enzyme activity. Therefore, we designed several control experiments by exposing native RNase A under different conditions (see the Experimental Section in the Supporting Information). As shown in Figure S5 (Supporting Information), RNase A retained 80%–85% of activity after incubation with $MgCl_2$-containing buffers at 30°C for 20 h compared with other buffers in the absence of $MgCl_2$. A high concentration of $MgCl_2$ (50×10^{-3} M) substantially decreased its initial activity (reduced to ≈25%), while incubation at 65 °C or the addition of DNF and Mg_2PPi had no pronounced effects on enzyme activity (Figure S6, Supporting Information). Given that the concentration of magnesium ions in DNF-R would be much less than 10×10^{-3} M (based on the data from Figure S2b, Supporting Information), these results allowed us to rationalize that the reduced activity of the encapsulated enzyme compared to free enzyme was predominantly due to the limited diffusion of the encapsulated enzyme by the surrounding DNA and Mg_2PPi.

To utilize DNA constructs as an intracellular delivery platform, it is crucial to ensure that they do not get digested by several nucleases in physiological conditions. With this purpose, serum stability was tested by incubating DNF, DNF-B, and DNF-R (0.1 μg of DNA) in the endothelial cell growth medium-2 (EGM-2) containing fetal bovine serum (FBS, 2% v/v) at 37 °C for 4, 8, 24, and 48 h and then resolved using agarose gel electrophoresis (Figure S7a, Supporting Information). The DNF and protein-DNF showed some resistance to serum degradation over a 48 h period, as evidenced by the existence of their representative bands with comparable band intensity to nontreated samples. In contrast, lambda DNA (λ-DNA) as a natural double-stranded DNA configuration was completely degraded within 48 h. This is consistent with the previous findings on the stability of RCA- or RCT-based synthetic DNA structures against nuclease degradation.[9b,10b,c] To further investigate their structural integrity, the particles with 24 h incubation were washed with nuclease-free water and visualized by SEM. The SEM images clearly showed that the particles still maintain the hierarchical original DNF with no apparent damage to the structure (Figure S7b, Supporting Information), ascertaining the potential of protein-embedded DNF for protein delivery systems.

Finally, we employed the DNF system to deliver cytotoxic RNase A to the cytoplasm of human cells as a proof of concept

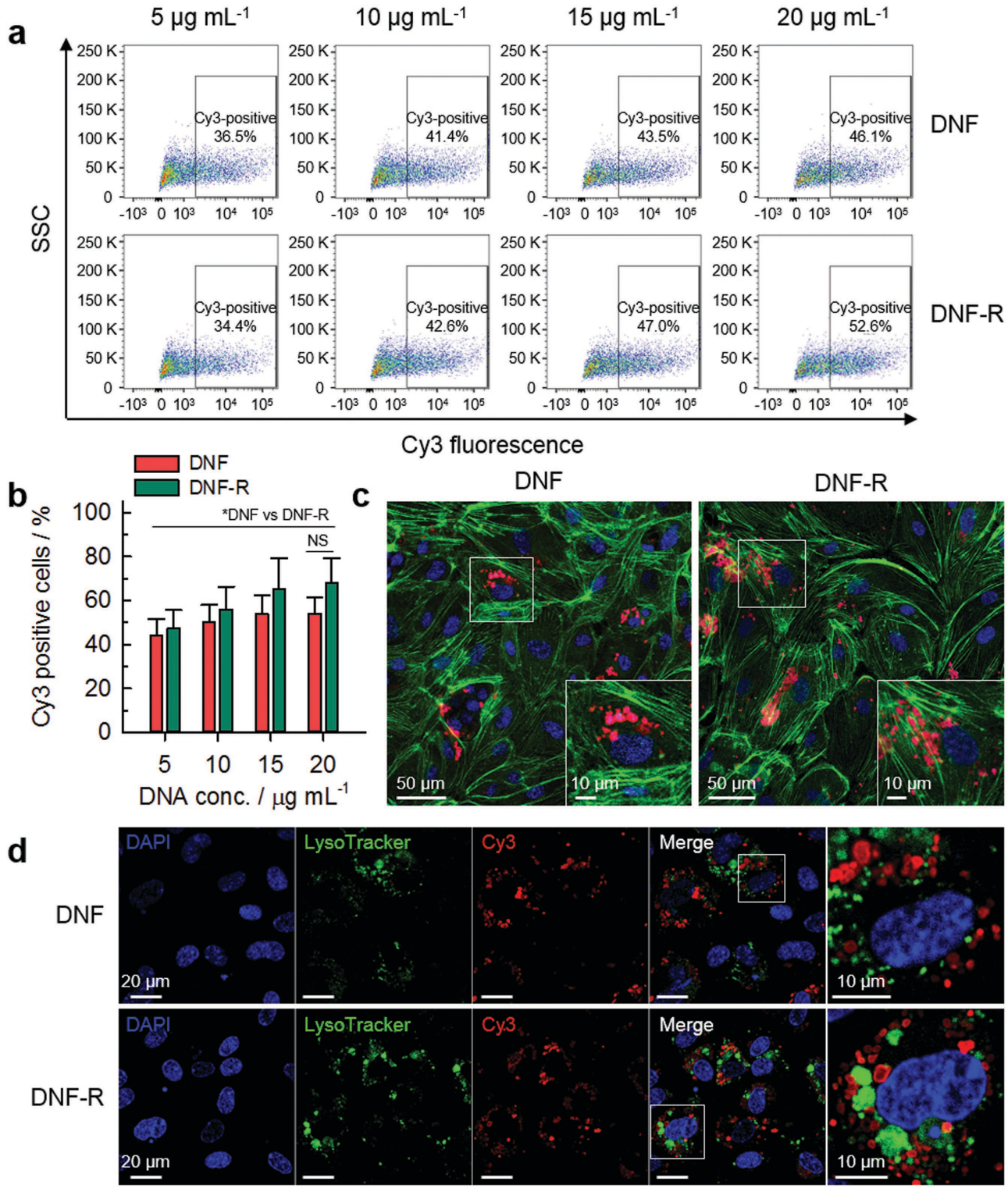

Figure 4. Cellular uptake of DNF-R by flow cytometry analysis and confocal microscopy. a) Representative dot plots of side scatter (SSC) versus Cy3 fluorescence intensity of HUVECs after treatment with Cy3-labelled DNF and DNF-R with increasing concentrations of DNA (5–20 μg mL^{-1}) at 37 °C for 24 h. Dead cells were distinguished using eFluor-450 and omitted from the analysis. b) Percentage of Cy3-positive cells. Data represent mean ± s.d. of three biological replicates. *$P < 0.05$, DNF versus DNF-R treated groups based on two-way ANOVA and Tukey's multiple comparison test; NS (not significant, $P > 0.05$) based on one-way ANOVA and Tukey's multiple comparison test. c) Internalization of Cy3-labeled DNF and DNF-R (15 μg mL^{-1} of DNA, red) into HUVECs at 24 h after incubation. The cells were counterstained with DAPI (blue, nucleus) and Alexa Fluor 488 phalloidin (green, actin). Insets show they retained their structural integrity with spherical shape. d) Intracellular colocalization of DNF and DNF-R with lysosomes. HUVECs were treated with Cy3-labeled DNF and DNF-R (15 μg mL^{-1} of DNA, red) for 24 h and stained with DAPI (blue, nucleus) and LysoTracker Green (green, lysosomes).

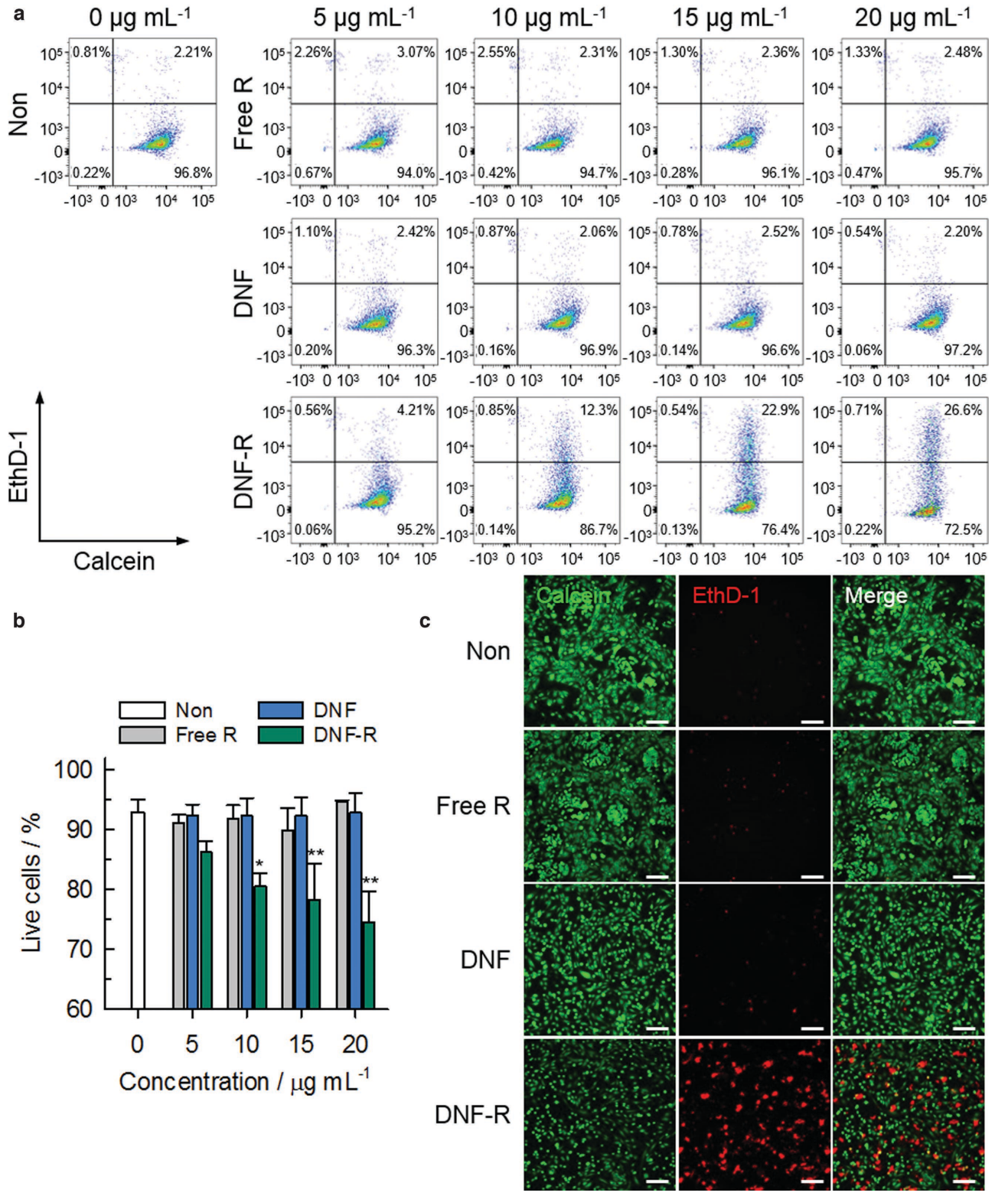

Figure 5. Cytotoxic effect of DNF-R. a) Representative dot plots of calcein fluorescence versus EthD-1 fluorescence of HUVECs by flow cytometry analysis. The cells were exposed to increasing concentrations of free R, DNF, and DNF-R at 37 °C for 24 h with poststaining with calcein AM and EthD-1. b) Percentages of live cells, based on the population of calcein-positive cells. Data represent mean ± s.d. of three biological replicates. $^{*}P < 0.005$, $^{**}P < 0.0001$ compared with nontreated cells based on one-way ANOVA and Tukey's multiple comparison test. c) Widefield microscopy images of HUVECs after treatment with free R, DNF, and DNF-R (15 μg mL^{-1} of RNase A in free R and DNF-R, 15 μg mL^{-1} of DNA in DNF) for 24 h, followed by dual staining of calcein AM and EthD-1 to discriminate live (green) and dead cells (red). Non, nontreatment; free R, free RNase A. Scale bar, 50 μm.

for protein delivery. As a cellular uptake and association study, Cy3-labeled DNF and DNF-R with different concentrations (5–20 μg mL^{-1} of DNA) were exposed to human umbilical vein endothelial cells (HUVECs) at 37 °C for 24 h. The uptake efficiency was determined based on the single cell population exhibiting red fluorescence using flow cytometry analysis. The results showed concentration-dependent Cy3-positive cells up to 46.1% and 52.6% for the DNF and the DNF-R at 20 μg mL^{-1} of DNA, respectively (**Figure 4**a,b). We note that the DNF-R displayed a slightly enhanced uptake efficiency compared to the DNF, although they had nearly identical sizes and zeta potentials (as shown in Figure 3b,c) which play an important role in particle internalization in combination with other factors such as material or cell types.[29] This difference is perhaps due to the presence of RNase A on the surface of DNF as many pancreatic-type ribonucleases have been proposed to interact with heparin sulfate proteoglycans linked to the cell membrane.[30] This effect appears consistent with previous findings showing that certain proteins adsorbed onto DNA-modified nanoparticles can control their cellular uptake.[31] However, additional in-depth studies on the uptake pathways of these materials need to be examined.

The intracellular distribution of both formulations observed by confocal microscopy was in qualitative agreement with the trends of uptake efficiency measured by flow cytometry analysis (Figure 4c). Since the DNF constructs were directly labeled during their synthesis by incorporation of fluorescent deoxynucleotide building blocks into the growing DNA strands, each DNF particle itself can be represented as a fluorescent dot. In the confocal microscopy images in Figure 4c,d, the red dots reflecting each Cy3-labeled particle were clearly seen in the cytoplasm, indicating that the structure of the internalized DNF particles remained topologically intact. Although DNA nanostructures have an intrinsic susceptibility to nuclease attack, there have been many reports in the literature proving their outstanding structural stability in physiological settings such as the extended exposure to cell lysates or cellular internalization.[32] In particular, Perrault and co-workers have reported that DNA nanostructures can be sensitive to depletion of magnesium ions and FBS nucleases in cell culture media, causing denaturation, and digestion of the nanostructures.[33] In light of this, such structural integrity within the cells could presumably be due to the relatively low concentration of FBS (2% v/v) in the media and the Mg_2PPi components in the DNF and DNF-R, which would prevent their denaturation and degradation by maintaining compact organization with DNA during intracellular uptake. More importantly, the majority of the red fluorescence of DNF and DNF-R was not colocalized with LysoTracker green in the cells after 24 h, suggesting that they were not accumulated in lysosomes (Figure 4d). We also recognize that DNF and DNF-R have limited uptake efficiency by cells, possibly due to their micron size, anionic charge, and some degree of sensitivity to the cellular condition. This could potentially be circumvented by customizing and protecting them with the aid of cationic agents,[9a,b,11] targeting ligands such as aptamers,[10a,b,34] peptides,[3a] and folic acid,[3a,12] and/or protective capping materials[35] for delivery purposes.

The therapeutic potential of DNF-R was evaluated using a LIVE/DEAD™ cell viability assay that allows simultaneous detection of live and dead cells with two color fluorescent probes, calcein acetoxymethyl ester (AM), and ethidium homodimer-1 (EthD-1).[36] Various concentrations of free RNase A and DNF-R (5–20 μg mL^{-1} of RNase A) and DNF alone (5–20 μg mL^{-1} of DNA) were treated with HUVECs at 37 °C for 24 h. As shown in **Figure 5**a,b, the resulting dot plots by flow cytometry showed live (calcein positive), dead (EthD-1 positive), and intermediate state (both calcein and EthD-1 positive) cell populations for each treatment. This pattern of intermediate state can be related to the fact that dead cells become double stained due to the damage on the cell outer membrane. Based on the percentage of live cells, we confirmed a concentration-dependent decrease in cell viability for DNF-R, whereas there were no observable cytotoxic effects for free enzyme and DNF (>90% cell viability). This is further supported by widefield microscopy images, showing that more dead cells (red) were detected in DNF-R-treated cells compared with the other controls (Figure 5c). Therefore, the results clearly demonstrate that the cytotoxic protein-loaded DNF are able to be delivered into the cell at concentrations sufficient to induce cell death.

In conclusion, we have developed protein–inorganic hybrid flowers using the well-established RCA technique that allows highly efficient protein loading while retaining the biological activity of the payloads. To the best of our knowledge, this system represents the first example of RCA-driven direct immobilization of multiple proteins in DNA constructs where the protein localization is fully dependent on its isoelectric point. The versatility of this method was ascertained by loading a given protein, including BSA, RNase A, and cytochrome C, onto the DNF under the biologically preferential condition. In particular, RNase A-containing DNF showed apparent catalytic activity with enhanced structural stability in physiological environments. With DNF-R, we could achieve effective RNase A delivery into HUVECs, thereby inducing significant cytotoxic effects compared to the free enzyme. Therefore, our strategy provides a simple and robust method for the direct encapsulation of various bioactive proteins and other macromolecules such as DNA. Given a variety of proteins and expanded selections of DNA with a combination of their inherent functions and chemical and physical properties, this approach will open up new opportunities to develop multifunctional materials that would impact biosensors, biocatalysis, bioimaging, and the delivery of therapeutics.

Supporting Information

Supporting Information is available from the Wiley Online Library or from the author. Raw data supporting this study is available online at DOI: 10.5281/zenodo.321252.

Acknowledgements

E.K. acknowledges support from Basic Science Research Program through the National Research Foundation of Korea (NRF) funded by the Ministry of Education (2015R1A6A3A03018919). L.Z.D. acknowledges support from the European Union's Horizon 2020 Research and Innovation Programme through the Marie Skłodowska-Curie Individual Fellowship "Magnetic HEART" under grant agreement no. 659175. C.S.H. was supported by a Ph.D. studentship of the EPSRC Centre for Doctoral Training under the Institute of Chemical Biology, Imperial College London (EP/L015498/1). S.A. gratefully acknowledges support

from the BHF Centre of Research Excellence (RE/08/002/23906). M.M.S., N.R., and E.K. acknowledge the ERC Seventh Framework Programme Consolidator grant "Naturale CG" under grant agreement no. 616417 and the grant "Bio-functionalized Nanomaterials for Ultrasensitive Biosensing" (EP/K020641/1) funded by EPSRC. The authors would like to thank the Facility for Imaging by Light Microscopy at Imperial College London for support with SIM and confocal imaging and the Flow Cytometry Facility at Imperial College London for assistance with the flow cytometry experiments.

Conflict of Interest

The authors declare no conflict of interest.

Keywords

cytotoxicity, DNA flowers, one-pot synthesis, protein delivery, protein encapsulation

Received: February 23, 2017
Revised: March 30, 2017
Published online:

[1] a) F. A. Aldaye, A. L. Palmer, H. F. Sleiman, *Science* **2008**, *321*, 1795; b) M. R. Jones, N. C. Seeman, C. A. Mirkin, *Science* **2015**, *347*, 1260901.

[2] a) Q. Jiang, C. Song, J. Nangreave, X. Liu, L. Lin, D. Qiu, Z.-G. Wang, G. Zou, X. Liang, H. Yan, B. Ding, *J. Am. Chem. Soc.* **2012**, *134*, 13396; b) Q. Zhang, Q. Jiang, N. Li, L. Dai, Q. Liu, L. Song, J. Wang, Y. Li, J. Tian, B. Ding, Y. Du, *ACS Nano* **2014**, *8*, 6633.

[3] a) H. Lee, A. K. R. Lytton-Jean, Y. Chen, K. T. Love, A. I. Park, E. D. Karagiannis, A. Sehgal, W. Querbes, C. S. Zurenko, M. Jayaraman, C. G. Peng, K. Charisse, A. Borodovsky, M. Manoharan, J. S. Donahoe, J. Truelove, M. Nahrendorf, R. Langer, D. G. Anderson, *Nat. Nanotechnol.* **2012**, *7*, 389; b) K. E. Bujold, J. C. C. Hsu, H. F. Sleiman, *J. Am. Chem. Soc.* **2016**, *138*, 14030.

[4] a) J. Li, H. Pei, B. Zhu, L. Liang, M. Wei, Y. He, N. Chen, D. Li, Q. Huang, C. Fan, *ACS Nano* **2011**, *5*, 8783; b) V. J. Schüller, S. Heidegger, N. Sandholzer, P. C. Nickels, N. A. Suhartha, S. Endres, C. Bourquin, T. Liedl, *ACS Nano* **2011**, *5*, 9696; c) X. Liu, Y. Xu, T. Yu, C. Clifford, Y. Liu, H. Yan, Y. Chang, *Nano Lett.* **2012**, *12*, 4254.

[5] S. M. Douglas, I. Bachelet, G. M. Church, *Science* **2012**, *335*, 831.

[6] a) D. S. Lee, H. Qian, C. Y. Tay, D. T. Leong, *Chem. Soc. Rev.* **2016**, *45*, 4199; b) W. B. Rogers, W. M. Shih, V. N. Manoharan, *Nat. Rev. Mater.* **2016**, *1*, 16008.

[7] M. G. Mohsen, E. T. Kool, *Acc. Chem. Res.* **2016**, *49*, 2540.

[8] M. M. Ali, F. Li, Z. Zhang, K. Zhang, D.-K. Kang, J. A. Ankrum, X. C. Le, W. Zhao, *Chem. Soc. Rev.* **2014**, *43*, 3324.

[9] a) J. B. Lee, J. Hong, D. K. Bonner, Z. Poon, P. T. Hammond, *Nat. Mater.* **2012**, *11*, 316; b) Y. H. Roh, J. B. Lee, K. E. Shopsowitz, E. C. Dreaden, S. W. Morton, Z. Poon, J. Hong, I. Yamin, D. K. Bonner, P. T. Hammond, *ACS Nano* **2014**, *8*, 9767; c) Y. H. Roh, J. Z. Deng, E. C. Dreaden, J. H. Park, D. S. Yun, K. E. Shopsowitz, P. T. Hammond, *Angew. Chem., Int. Ed.* **2016**, *55*, 3347.

[10] a) G. Zhu, R. Hu, Z. Zhao, Z. Chen, X. Zhang, W. Tan, *J. Am. Chem. Soc.* **2013**, *135*, 16438; b) R. Hu, X. Zhang, Z. Zhao, G. Zhu, T. Chen, T. Fu, W. Tan, *Angew. Chem., Int. Ed.* **2014**, *53*, 5821; c) Y. Lv, R. Hu, G. Zhu, X. Zhang, L. Mei, Q. Liu, L. Qiu, C. Wu, W. Tan, *Nat. Protoc.* **2015**, *10*, 1508.

[11] W. Sun, W. Ji, J. M. Hall, Q. Hu, C. Wang, C. L. Beisel, Z. Gu, *Angew. Chem., Int. Ed.* **2015**, *54*, 12029.

[12] W. Sun, T. Jiang, Y. Lu, M. Reiff, R. Mo, Z. Gu, *J. Am. Chem. Soc.* **2014**, *136*, 14722.

[13] C. Wang, W. Sun, G. Wright, A. Z. Wang, Z. Gu, *Adv. Mater.* **2016**, *28*, 8912.

[14] Z. Zhao, J. Fu, S. Dhakal, A. Johnson-Buck, M. Liu, T. Zhang, N. W. Woodbury, Y. Liu, N. G. Walter, H. Yan, *Nat. Commun.* **2016**, *7*, 10619.

[15] W. Sun, W. Ji, Q. Hu, J. Yu, C. Wang, C. Qian, G. Hochu, Z. Gu, *Biomaterials* **2016**, *96*, 1.

[16] Y. I. Tarasevich, *Theor. Exp. Chem.* **2001**, *37*, 98.

[17] a) G. Kartha, J. Bello, D. Harker, *Nature* **1967**, *213*, 862; b) R. Ravindra, S. Zhao, H. Gies, R. Winter, *J. Am. Chem. Soc.* **2004**, *126*, 12224.

[18] P. A. Leland, L. W. Schultz, B.-M. Kim, R. T. Raines, *Proc. Natl. Acad. Sci. USA* **1998**, *95*, 10407.

[19] Y. Mori, K. Nagamine, N. Tomita, T. Notomi, *Biochem. Biophys. Res. Commun.* **2001**, *289*, 150.

[20] a) J. A. W. Heymann, M. Hayles, I. Gestmann, L. A. Giannuzzi, B. Lich, S. Subramaniam, *J. Struct. Biol.* **2006**, *155*, 63; b) N. Reznikov, R. Shahar, S. Weiner, *Bone* **2014**, *59*, 93.

[21] a) L. Schermelleh, P. M. Carlton, S. Haase, L. Shao, L. Winoto, P. Kner, B. Burke, M. C. Cardoso, D. A. Agard, M. G. L. Gustafsson, H. Leonhardt, J. W. Sedat, *Science* **2008**, *320*, 1332; b) B. Huang, H. Babcock, X. Zhuang, *Cell* **2010**, *143*, 1047.

[22] R. E. Dickerson, T. Takano, D. Eisenberg, O. B. Kallai, L. Samson, A. Cooper, E. Margoliash, *J. Biol. Chem.* **1971**, *246*, 1511.

[23] C. B. Black, H. W. Huang, J. A. Cowan, *Coord. Chem. Rev.* **1994**, *135*, 165.

[24] a) C. A. Kreader, *Appl. Environ. Microbiol.* **1996**, *62*, 1102; b) M. Nagai, A. Yoshida, N. Sato, *IUBMB Life* **1998**, *44*, 157.

[25] a) P. M. Lizardi, X. Huang, Z. Zhu, P. Bray-Ward, D. C. Thomas, D. C. Ward, *Nat. Genet.* **1998**, *19*, 225; b) J. Jarvius, J. Melin, J. Goransson, J. Stenberg, S. Fredriksson, C. Gonzalez-Rey, S. Bertilsson, M. Nilsson, *Nat. Methods* **2006**, *3*, 725.

[26] N. J. Greenfield, *Nat. Protoc.* **2007**, *1*, 2876.

[27] J. Kypr, I. Kejnovská, D. Renčiuk, M. Vorlíčková, *Nucleic Acids Res.* **2009**, *37*, 1713.

[28] a) D. Feng, T.-F. Liu, J. Su, M. Bosch, Z. Wei, W. Wan, D. Yuan, Y.-P. Chen, X. Wang, K. Wang, X. Lian, Z.-Y. Gu, J. Park, X. Zou, H.-C. Zhou, *Nat. Commun.* **2015**, *6*, 5979; b) F.-K. Shieh, S.-C. Wang, C.-I. Yen, C.-C. Wu, S. Dutta, L.-Y. Chou, J. V. Morabito, P. Hu, M.-H. Hsu, K. C. W. Wu, C.-K. Tsung, *J. Am. Chem. Soc.* **2015**, *137*, 4276; c) G. Song, Y. Chen, C. Liang, X. Yi, J. Liu, X. Sun, S. Shen, K. Yang, Z. Liu, *Adv. Mater.* **2016**, *28*, 7143.

[29] J. Wang, J. D. Byrne, M. E. Napier, J. M. DeSimone, *Small* **2011**, *7*, 1919.

[30] T.-Y. Chao, R. T. Raines, *Biochemistry* **2011**, *50*, 8374.

[31] D. A. Giljohann, D. S. Seferos, P. C. Patel, J. E. Millstone, N. L. Rosi, C. A. Mirkin, *Nano Lett.* **2007**, *7*, 3818.

[32] a) Q. Mei, X. Wei, F. Su, Y. Liu, C. Youngbull, R. Johnson, S. Lindsay, H. Yan, D. Meldrum, *Nano Lett.* **2011**, *11*, 1477; b) A. S. Walsh, H. Yin, C. M. Erben, M. J. A. Wood, A. J. Turberfield, *ACS Nano* **2011**, *5*, 5427.

[33] J. Hahn, S. F. J. Wickham, W. M. Shih, S. D. Perrault, *ACS Nano* **2014**, *8*, 8765.

[34] C. Wu, D. Han, T. Chen, L. Peng, G. Zhu, M. You, L. Qiu, K. Sefah, X. Zhang, W. Tan, *J. Am. Chem. Soc.* **2013**, *135*, 18644.

[35] a) J. Mikkilä, A.-P. Eskelinen, E. H. Niemelä, V. Linko, M. J. Frilander, P. Törmä, M. A. Kostiainen, *Nano Lett.* **2014**, *14*, 2196; b) S. D. Perrault, W. M. Shih, *ACS Nano* **2014**, *8*, 5132.

[36] N. G. Papadopoulos, G. V. Z. Dedoussis, G. Spanakos, A. D. Gritzapis, C. N. Baxevanis, M. Papamichail, *J. Immunol. Methods* **1994**, *177*, 101.